ADVANCED ENERGY MATERIALS
www.advenergymat.de

# A General Strategy to Boost Electrocatalytic Nitrogen Reduction on Perovskite Oxides via the Oxygen Vacancies Derived from A-Site Deficiency

*Kaibin Chu, Fuzhu Liu, Jiawei Zhu,* Hui Fu, Haiyan Zhu, Yinlong Zhu, Yu Zhang, Feili Lai, and Tianxi Liu**

**The electrocatalytic $N_2$ reduction reaction (NRR) under ambient conditions is an attractive strategy for green synthesis of $NH_3$. Due to the ultra-stable N≡N covalent triple bond, it is very challenging to develop highly selective and efficient electrocatalysts toward NRR. Here a general strategy to enhance the NRR activity through modulating A-site-deficiency-induced oxygen vacancies of perovskite oxides is reported. One successful example is $La_xFeO_{3-\delta}$ ($L_xF$, $x = 1$, 0.95, and 0.9) perovskite oxides with tunable oxygen vacancies that are directly proportional to the La-site deficiencies. As compared to the pristine LF, the $L_{0.95}F$ and $L_{0.9}F$ exhibit significantly improved NRR activities, which are positively correlated with the La-site deficiency and the amount of oxygen vacancies. Among them, the $L_{0.9}F$ delivers the best activity, with an $NH_3$ yield rate of 22.1 $\mu g \cdot h^{-1} \cdot mg^{-1}_{cat.}$ at −0.5 V and a Faradaic efficiency of 25.6% at −0.3 V, which are 2.2 and 1.6 times those of the pristine LF, respectively. Both experimental characterizations and theoretical calculations suggest that the enhanced NRR activity can be mainly attributed to the favorable merits produced by the oxygen vacancies: the promoted adsorption/activation of reaction species, and thus optimized reaction pathways. Application of this strategy to other perovskite oxides generates similarly successful results.**

## 1. Introduction

Ammonia ($NH_3$) plays an essential role in our modern society owing to its remarkable impact on agriculture, medicine, chemicals, and energy.[1,2] The industrial-scale production of $NH_3$ has been achieved through Haber–Bosch process since 1908. However, this process not only operates under harsh environments involving high temperatures (400–500 °C) and pressures (10–30 MPa), but also demands a large deal of $H_2$ mainly from natural gas reforming which causes abundant consumption of fossil fuels and huge $CO_2$ emissions.[3–6] As a result, for energy conservation and environmental protection, it is of crucial importance to explore a clean and sustainable route for $NH_3$ production. Electrocatalytic $N_2$ reduction reaction (NRR) under ambient conditions has been emerged recently as an attractive strategy for the green synthesis of $NH_3$ through utilizing inexhaustible $N_2$ and $H_2O$.[7–12] However, due to the competition with $H_2$ evolution reaction (HER) and ultra-stable N≡N covalent triple bond, NRR suffers from unsatisfactory Faradaic efficiency (FE) and sluggish reaction kinetics.[13] It is of eager desire, but very challenging to develop selective and efficient electrocatalysts toward NRR that can inhibit the competitive HER and activate the $N_2$ molecule.

Among various developed electrocatalysts, perovskite oxides have proven their great potential toward NRR because of their low cost, good adjustability in intriguing physicochemical properties, as well as economic and environmental friendliness. Typical examples include a few simple perovskite oxides, such as $LaCoO_3$, $LaCrO_3$, $LaFeO_3$, $La_2Ti_2O_7$, and $Ce_{1/3}NbO_3$.[14–19] Although significant progress has been made, their NRR performance is still far from the requirements of commercial $NH_3$ synthesis. Most recently, several studies have shown that the electrocatalytic

K. Chu, Prof. J. Zhu, H. Fu, H. Zhu, Prof. T. Liu
Key Laboratory of Synthetic and Biological Colloids
Ministry of Education
School of Chemical and Material Engineering
Jiangnan University
Wuxi, Jiangsu 214122, P. R. China
E-mail: jwzhu@jiangnan.edu.cn; txliu@jiangnan.edu.cn
Dr. F. Liu
State Key Laboratory for Mechanical Behavior of Materials
Xi'an Jiaotong University
Xi'an, Shanxi 710049, P. R. China
The ORCID identification number(s) for the author(s) of this article can be found under https://doi.org/10.1002/aenm.202003799.
Dr. Y. Zhu
Department of Chemical Engineering
Monash University
Clayton, Victoria 3800, Australia
Dr. Y. Zhang
School of Mechanical and Power Engineering
East China University of Science and Technology
130 Meilong Road, Shanghai 200237, P. R. China
Dr. F. Lai
Department of Chemistry
KU Leuven
Celestijnenlaan 200F, Leuven 3001, Belgium

DOI: 10.1002/aenm.202003799

 

activities toward NRR and others (e.g., oxygen evolution, hydrogen evolution) of perovskite oxides can be effectively enhanced through oxygen vacancy engineering.[20–26] The main mechanism has been certified to be that B-site cations combining with their adjacent oxygen vacancies can serve as unsaturated active centers that strengthen the ability to adsorb/activate $N_2$ molecule and thus lead NRR on the optimal reaction pathway.[14] Despite these efforts, their preparation methods involving special atmosphere (e.g., 5% $H_2$/Ar) annealing had made it challenging to rationally tailor the oxygen vacancies, not mentioning the instability of most of the perovskite oxides under those conditions.[27–29] Such methods are not well-suited for the development of highly active perovskite oxides for NRR. To this end, there is an urgent need to construct oxygen vacancies simply but reliably in perovskite oxides to maximize their NRR activity. Alternatively, the A-site deficiencies in perovskite lattice could automatically derive tunable oxygen vacancies, and thereby alter the physicochemical properties.[30,31] However, to our knowledge, the effect of such A-site-deficiency-derived oxygen vacancies on the NRR activity is not yet to be fully investigated.

Here we report a general strategy based on the introduction of A-site deficiency for controlling the oxygen vacancies and thus enhancing the electrocatalytic NRR activity of perovskite oxides. As the proof of concept, we synthesized $La_xFeO_{3-\delta}$ ($x$ = 0.95 and 0.9) nanoparticles, labeled as $L_{0.95}F$ and $L_{0.9}F$, respectively, with controllable amounts of oxygen vacancies, by easily tuning the La-site deficiencies in $LaFeO_{3-\delta}$ nanoparticles (denoted LF). When evaluated as electrocatalysts toward NRR, relative to its parent LF, the $L_{0.95}F$ and $L_{0.9}F$ exhibited substantially enhanced activities that were positively correlated with the quantity of oxygen vacancies. Among the samples, the $L_{0.9}F$ with the most oxygen vacancies featured the maximal activities and excellent durability. Our experimental characterizations and theoretical calculations both suggested that establishing more oxygen vacancies in perovskite oxides could further modulate the intermediate adsorption, facilitate $N_2$ molecule activation, together with optimizing the potential-determining step, and thereby contribute to the well-boosted NRR performance. We further demonstrated the generality of this strategy by extending it to other representative perovskite oxides, including $SrCo_{0.5}Fe_{0.5}O_{3-\delta}$ (SCF) versus $Sr_{0.95}Co_{0.5}Fe_{0.5}O_{3-\delta}$ ($S_{0.95}$CF), and $SrFe_{0.9}Ta_{0.1}O_{3-\delta}$ (SFT) versus $Sr_{0.95}Fe_{0.9}Ta_{0.1}O_{3-\delta}$ ($S_{0.95}$FT) nanoparticles. As expected, these A-site deficient perovskite oxides of $S_{0.95}$CF and $S_{0.95}$FT also showed highly improved NRR activities as compared to the pristine SCF and SFT, respectively.

## 2. Results and Discussion

We prepared the LF, $L_{0.95}F$, and $L_{0.9}F$ nanoparticles through gradually reducing the added amounts of lanthanum nitrate in the synthesis process. According to our inductively coupled plasma mass spectroscopy (ICP-MS) analysis, the bulk compositions of the LF, $L_{0.95}F$, and $L_{0.9}F$ samples are consistent with the intended compositions (Table S1, Supporting Information). **Figure 1**a shows X-ray diffraction (XRD) patterns of the LF, $L_{0.95}F$, and $L_{0.9}F$ nanoparticles. All of these samples exhibited a pure orthorhombic crystal structure sharing a space group of Pnma (JCPDS, No. 88-0641). As the concentration of A-site deficiency increased, the position of the main peak corresponding to (121) plane slightly shifted to higher angle, suggesting a lattice shrinkage, which could be probably attributed to the tilted $FeO_6$ octahedra to fill the extra space created by the La-site

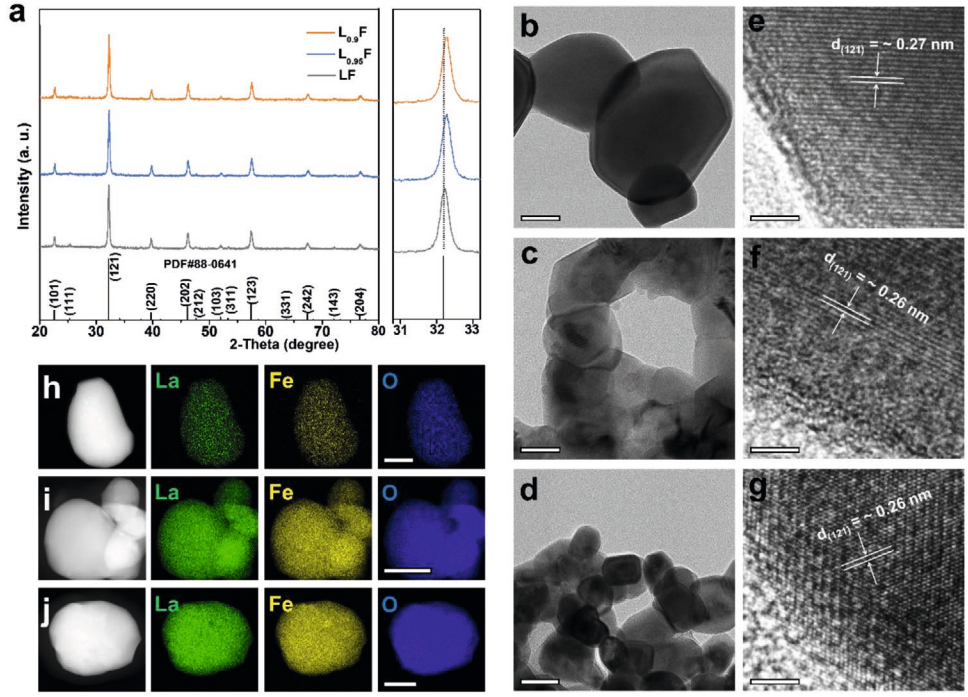


**Figure 1.** a) XRD patterns of LF, $L_{0.95}F$, and $L_{0.9}F$. b–d) TEM images of LF (b), $L_{0.95}F$ (c), and $L_{0.9}F$ (d) (scale bar: 50 nm). e–g) HRTEM images of LF (e), $L_{0.95}F$ (f), and $L_{0.9}F$ (g) (scale bar: 5 nm). h–j) EDX mappings of LF (h), $L_{0.95}F$ (i), and $L_{0.9}F$ (j) (scale bar: 100 nm).

deficiency.[32] As a note, because more La-site deficiencies (i.e., 15% and even higher) in LF could produce an impurity phase of $Fe_2O_3$, here we limited the La-site deficiency to 10% for avoiding the effects of impurity phase on NRR activity.[33,34] Scanning electron microscopy (SEM) (Figure S1, Supporting Information) and transmission electron microscopy (TEM) (Figure S2, Supporting Information and Figure 1b–d) images showed typical morphologies of the LF, $L_{0.95}F$, and $L_{0.9}F$ nanoparticles. For all of these samples, the average particle sizes were around 55–65 nm (Figure S3, Supporting Information) that hardly changed with the variations in A-site deficiency. As displayed in Figure S4, the Brunauer–Emmett–Teller specific surface areas of the LF, $L_{0.95}F$, and $L_{0.9}F$ nanoparticles were nearly the same of around 24 $m^2\ g^{-1}$, indicating that the three samples exhibited similar particle sizes that were consistent with the SEM and TEM results. Figure 1e–g shows high resolution TEM (HRTEM) images of the three samples. The clear crystal fringes with lattice spacings of about 0.27, 0.26, and 0.26 nm (for LF, $L_{0.95}F$, and $L_{0.9}F$ samples, respectively) belonged to the (121) diffraction plane of perovskite oxides with an orthorhombic crystal structure. The energy dispersive X-ray (EDX) mapping in Figure 1h–j suggested the uniform distribution of La, Fe, and O elements in the LF, $L_{0.95}F$, and $L_{0.9}F$ nanoparticles. The X-ray photoelectron spectra (XPS) of these samples further validated that these three samples were composed of La, Fe, and O elements (Figure S5, Supporting Information) without any detected N signal (Figure S6, Supporting Information), excluding the disturbance of N element on the following NRR test.

We performed XPS, iodometric titration, and electron paramagnetic resonance (EPR) to clarify the relationship between the oxygen vacancies and La-site deficiencies in the three samples. **Figure 2**a shows O 1s XPS spectra of LF, $L_{0.95}F$, and $L_{0.9}F$. The peaks at 528.8, 530.4, 531.3, and 532.7eV were assigned to lattice $O^{2-}$, highly oxidative oxygen species ($O_2^{2-}/O^-$), surface-adsorbed $O_2$ or hydroxyl groups, and surface-adsorbed $H_2O$,

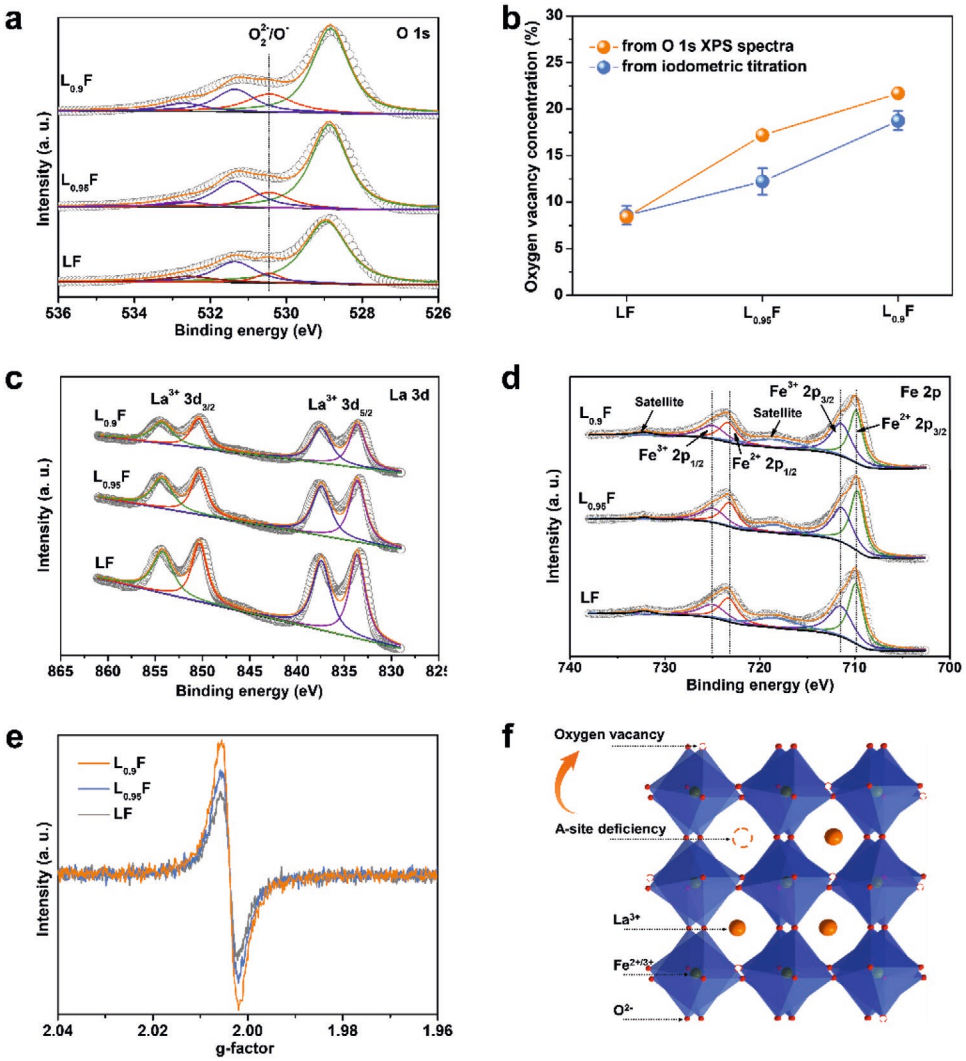


**Figure 2.** a) O 1s XPS spectra of the LF, $L_{0.95}F$, and $L_{0.9}F$. b) Oxygen vacancy concentrations of the LF, $L_{0.95}F$, and $L_{0.9}F$ obtained from O 1s XPS spectra and iodometric titration. c) La 3d XPS spectra of the LF, $L_{0.95}F$, and $L_{0.9}F$. d) Fe 2p XPS spectra of the LF, $L_{0.95}F$, and $L_{0.9}F$. e) EPR spectra of the LF, $L_{0.95}F$, and $L_{0.9}F$. f) Schematic illustration of the generation of oxygen vacancies in A-site-deficient $L_xF$.

respectively.[33] Based on the relative areas of their peaks, the surface oxygen vacancy (correlated with the $O_2^{2-}/O^-$ species) concentrations of the LF, $L_{0.95}F$, and $L_{0.9}F$ samples were calculated to be 8.5%, 17.2%, and 21.7%, respectively, suggesting that the surface oxygen vacancies increased with La-site deficiencies (Figure 2b and Table S2, Supporting Information). In the iodometric titration experiments, for the LF (8.6%), $L_{0.95}F$ (12.2%), and $L_{0.9}F$ (18.7%) samples (Figure 2b), we obtained a similar change trend of oxygen vacancies to that in the XPS analysis. It should be noted that, mainly due to the different properties in the surface and bulk, there is a gap in these oxygen vacancy concentration values determined by these two methods. Such change patterns of the oxygen vacancies in these samples were further verified by La 3d and Fe 2p XPS spectra (Figure 2c,d). The valence state of La (+3) in these samples were unchanged (Figure 2c), while the average valence states of Fe in the LF, $L_{0.95}F$, and $L_{0.9}F$ showed small changes, with the corresponding values of +2.53, +2.47, and +2.49, respectively. (Figure 2d and Table S3, Supporting Information). As a result, according to the electroneutrality principle, the $L_xF$ with more A-site deficiencies was equipped with more oxygen vacancies. As shown in Figure 2e, the LF, $L_{0.95}F$, and $L_{0.9}F$ displayed EPR signals at $g = 2.003$, of which the intensity was directly proportional to oxygen vacancy content. The intensity of the EPR signals decreased in the following order: $L_{0.9}F > L_{0.95}F >$ LF, indicating that a higher concentration of oxygen vacancies could be produced by introducing more La-site deficiencies. Taken together, engineering La-site deficiency in LF was able to rationally manipulate the surface oxygen vacancies (Figure 2f).

The electrocatalytic NRR properties of the LF, $L_{0.95}F$, and $L_{0.9}F$ nanoparticles were evaluated in a typical H-type cell under ambient conditions using 0.1 M $Li_2SO_4$ aqueous solution (pH = 6.22) as the electrolyte. We applied the indophenol blue and Watt–Chrisp methods to quantitatively determine the $NH_3$ product and the possible byproduct $N_2H_4$, respectively, with the calibration curves shown in Figures S7 and S8, Supporting Information. To confirm the detection results by the indophenol blue method, we also performed the ion chromatography analysis at the highest $NH_3$ yield potential with the calibration curve shown in Figure S9, Supporting Information. Figure S10, Supporting Information shows linear sweep voltammogram curves recorded in Ar- and $N_2$-saturated electrolytes for these samples. In the potential range of –0.1 to –0.6 V, there was a higher current density in $N_2$-saturated electrolyte relative to that in Ar-saturated electrolyte, indicating that these samples were active toward NRR. We then conducted chronoamperometry tests (for 2 h, from –0.1 to –0.6 V) in $N_2$-saturated electrolyte as well as following ultraviolet–visible (UV–vis) absorption spectroscopy measurements to evaluate the NRR activity of these samples (Figures S11 and S12, Supporting Information). $NH_3$ yield rates and FEs for $NH_3$ of these samples exhibited volcano-type dependence on the applied potentials, with a maximum point corresponding to –0.5 and –0.3 V, respectively (**Figure 3**a,b). This phenomenon could be attributed to the combination of the stronger competition from HER at more negative potentials and the reduced amount of charges at more positive potentials. In the tested potential window, the $NH_3$ yield rates of these catalysts featured a direct correlation with the amount of La-site deficiencies or oxygen vacancies, complying with the following sequence: LF < $L_{0.95}F$ < $L_{0.9}F$ (Figure 3a and Figure S13, Supporting Information). Specifically, at –0.5 V, the $NH_3$ yield rates of the $L_{0.95}F$ (14.4 $\mu g \cdot h^{-1} \cdot mg^{-1}_{cat.}$) and $L_{0.9}F$ (22.1 $\mu g \cdot h^{-1} \cdot mg^{-1}_{cat.}$) showed about 1.4 and 2.2 times as high as that of the pristine LF (10.2 $\mu g \cdot h^{-1} \cdot mg^{-1}_{cat.}$) (Figure 3a and Figure S14, Supporting Information). In addition, in the tested potential range, the FEs of $L_{0.95}F$ and $L_{0.9}F$ mainly exceeded those of LF (Figure 3b). For example, at –0.3 V, the $L_{0.95}F$ and $L_{0.9}F$ exhibited remarkable FEs for $NH_3$ of 21.6% and 25.6%, respectively, both greater than that of the LF (16.5%). It is worth noting that no byproduct $N_2H_4$ was detected, confirming the excellent selectivity of these catalysts toward $NH_3$ electrosynthesis (Figure S15, Supporting Information). Therefore, one can readily optimize the NRR activities of the $L_xF$ catalysts by tuning their La-site deficiencies and thus oxygen vacancies.

Several control experiments were carried out to verify that the $NH_3$ was produced by NRR over these catalysts. Taking the $L_{0.9}F$ as an example, as shown in Figure 3c,d, at an open-circuit potential in $N_2$-saturated electrolyte, no obvious $NH_3$ was detected after NRR, suggesting no contamination of $NH_3$ from the feeding $N_2$ and the catalyst. When Ar replaced $N_2$ for NRR over the $L_{0.9}F$ catalyst, no obvious signal for $NH_3$ was detected, confirming that the catalyst itself did not produce $NH_3$ and the $NH_3$ was originated from electroreduction of the feeding $N_2$. Moreover, $NH_3$ was not detected when NRR was performed over a bare carbon paper, further ensuring that the $NH_3$ was produced by the $L_{0.9}F$ catalyst during NRR. Therefore, it was evidenced that the NRR over the catalysts contributed to those high $NH_3$ yield rates and FEs.

In addition to the significantly enhanced activity, the $L_{0.9}F$ catalyst exhibited excellent catalytic durability toward NRR. We evaluated the catalytic durability of the $L_{0.9}F$ through consecutive static repetitive tests at –0.5 V. During the five consecutive cycles of successive electrolysis, no obvious changes in current densities and absorbance of electrolytes were observed (Figure S16, Supporting Information). More importantly, both the $NH_3$ yield rate and FE showed no apparent decline (Figure 3e). We then characterized the crystal phase of the used $L_{0.9}F$ catalyst. The XRD patterns showed that the crystal phase of the $L_{0.9}F$ was well preserved after the durability test (Figure 3f). All the above results proved that the $L_{0.9}F$ catalyst was very stable in NRR conditions.

To explore the origin of the significant NRR activity of the A-site deficient perovskite oxides, we conducted a series of characterizations. We measured the double-layer capacitance ($C_{dl}$) values (correlated with electrochemical active surface area, ECSA) of these samples (Figure S17, Supporting Information). The $C_{dl}$ values of these samples only varied from 0.18 to 0.21 $mF \cdot cm^{-2}$ (**Figure 4**a). On this basis, the activity gap among the LF, $L_{0.95}F$, and $L_{0.9}F$ was not closely related to the ECSA. Figure 4b shows the Nyquist plots of the LF, $L_{0.95}F$, and $L_{0.9}F$ catalysts. As the content of A-site deficiency was increased, the charge transfer resistances for these samples were decreased. Accordingly, the catalysts with more A-site deficiencies or oxygen vacancies exhibited much faster electron transfer rates toward NRR. Furthermore, the adsorption properties (e.g., binding strength) of reaction intermediates on the catalytic sites are essential for the catalytic activity.[35] By using valence band XPS spectra, we obtained d-band center of these catalysts,

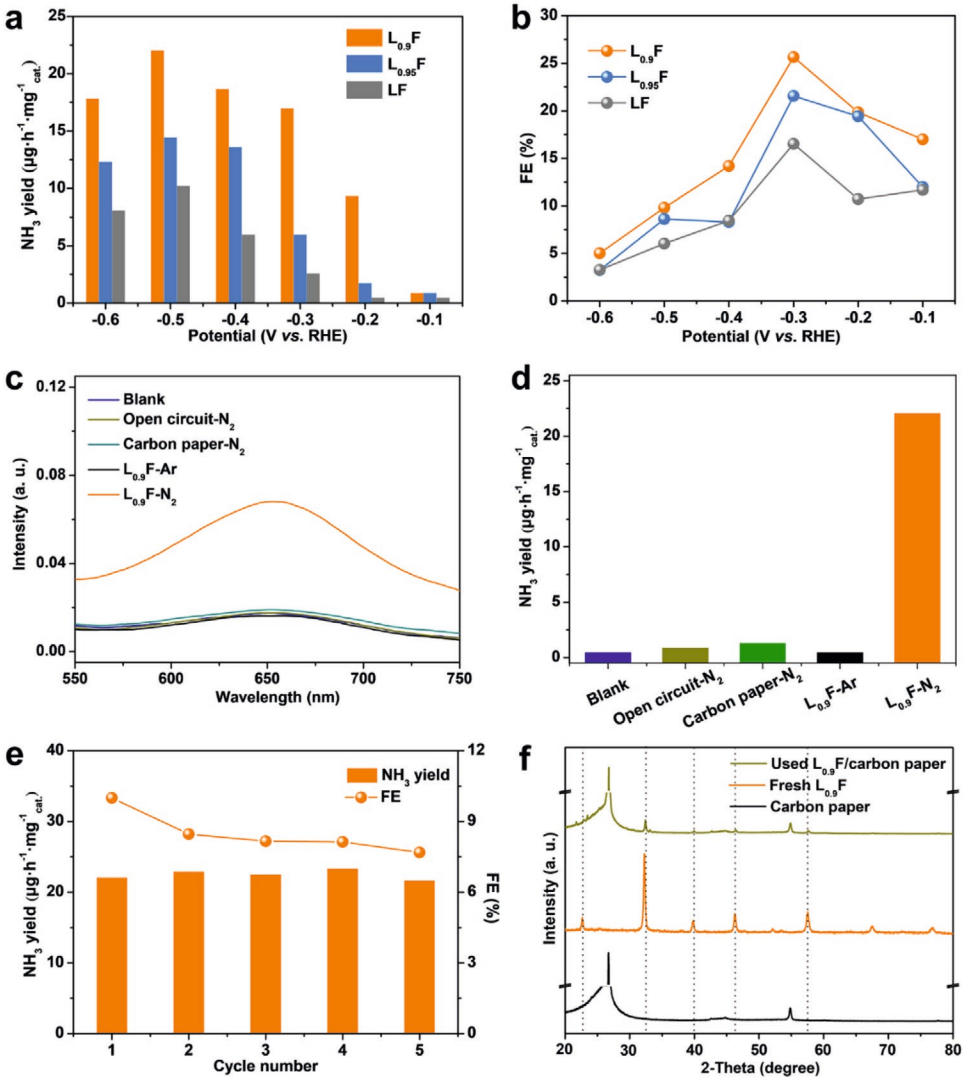


**Figure 3.** a) $NH_3$ yield rates and b) FEs at applied potentials over the LF, $L_{0.95}F$, and $L_{0.9}F$ catalysts (RHE: reversible hydrogen electrode). c) UV–visible absorption spectra of the electrolytes after electrolysis and d) the corresponding $NH_3$ yield rates under different conditions: at the open-circuit potential in $N_2$-saturated electrolyte, over the $L_{0.9}F$ catalyst in $N_2$- or Ar-saturated electrolyte at –0.5 V, and on a bare carbon in $N_2$-saturated electrolyte at –0.5 V. e) $NH_3$ yield rates and FEs of $L_{0.9}F$ after each consecutive cycle at –0.5 V. f) XRD patterns of the $L_{0.9}F$ after five consecutive cycles.

which was considered as a practical mean to describe the intermediate adsorption properties.[36] As revealed in Figure 4c, with the A-site deficiency or oxygen vacancy increasing, the d-band centers (relative to the Femi level) of the $L_xF$ gradually shifted upward, thereby probably leading to the strengthened adsorption of $N_2$ and its intermediates.[12] Among the samples, the $L_{0.9}F$ with the maximum amount of oxygen vacancies showed the highest d-band center and thus the strongest affinity for the adsorbed species. We also conducted $N_2$ temperature programmed desorption ($N_2$-TPD) to further prove the capacity of $N_2$ adsorption for these catalysts (Figure 4d). All of these samples featured desorption peaks at about 100.5 °C, which could be indexed to the physical adsorption signals for $N_2$ on the catalyst surfaces.[37] As expected, the starting temperature for desorption of chemisorbed $N_2$ increased in the following order: LF (264.4 °C) < $L_{0.95}F$ (289.6 °C) < $L_{0.9}F$ (325.4 °C), indicating an enhanced chemisorption of $N_2$ for A-site more deficient samples. The most plausible explanation was that, for the catalyst with more A-site deficiencies, more oxygen vacancies were formed, which brought more active sites for the chemisorption and activation of $N_2$ molecule. Hence, the introduction of A-site deficiency and thus oxygen vacancy into $L_xF$ could not only accelerate the electron transfer, but also effectively adsorb and activate $N_2$, thereby boosting the catalytic activity toward NRR.

We further performed density functional theory (DFT) calculations to understand the mechanism behind the excellent NRR activities over $L_xF$ with additional oxygen vacancy. The DFT calculations based on the computational hydrogen electrode model were implemented on the LF(121) and oxygen-vacancy-contained LF(121) (labeled as $O_v$-LF(121)) surfaces. **Figure 5** and Table S4, Supporting Information give Gibbs free energy ($\Delta G$) profiles for both LF(121) and $O_v$-LF(121) surfaces toward NRR. For the LF(121), the adsorption energy of $N_2$ was 0.28 eV, and the hydrogenation of $*N_2$ to *NNH ($\Delta G$ = 0.97 eV) was the

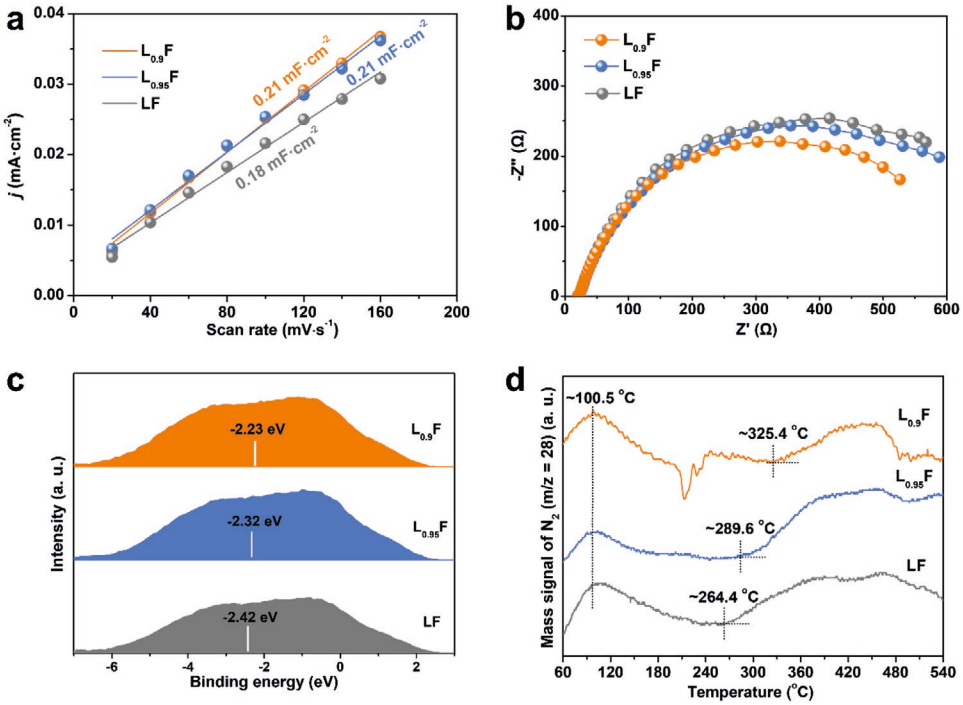


**Figure 4.** a) Linear fitting curves of the capacitive currents against scan rates for the catalysts. b) Nyquist plots of the catalysts. c) Surface valance band spectra of the catalysts. d) TPD-MS profiles of $N_2$ ($m/z = 28$) for the catalysts.

potential-determining step, indicating weak activation of $N_2$ molecule on the surface. In this case, the $*N_2$ and *NNH were adsorbed on the top of Fe atom (see insets in Figure 5) with the distance of 1.641 and 1.658 Å, respectively. This reaction mechanism was consistent with several previous studies focused on metal oxide surfaces (e.g., $TiO_2$(110) and $LaCoO_3$(111)).[14,38] While the surface oxygen vacancy was introduced, the coordination environment as well as the electronic properties was changed, and the adsorption properties of the reaction species were also modulated. For the $O_v$-LF(121), the $N_2$ molecule was also adsorbed on the top of Fe site instead of the vacancy site (Fe–Fe bridge site) over the surface. However, owing to the presence of oxygen vacancy, the $N_2$ adsorption energy (–0.296 eV) was lowered by 0.578 eV relative to the pristine LF(121), revealing that the $N_2$ adsorption was greatly strengthened. As the hydrogenation of $*NNH_2$ to $*NHNH_2$ showed the highest energy barrier of 0.46 eV, this step was considered as the potential-determining step for the $O_v$-LF(121) surface toward NRR, where the $*NNH_2$ and $*NHNH_2$ were adsorbed on the Fe site nearby the oxygen vacancy site (see insets in Figure 5) with distance of 1.521 and 1.646 Å, respectively. These results demonstrated that the introduction of oxygen vacancy into LF(121) surface could not only facilitate the adsorption and activation of the $N_2$ molecule, but also optimize the reaction pathways through intensifying the interaction between the adsorbed species and unsaturated Fe site. Noting that because the A-site cations in perovskite oxides usually did not play as the active sites toward catalysis,[30] the A-site deficiency was not considered in our $O_v$ model during calculating the reaction paths. Although there is a little difference (i.e., –0.04 and 0.16 eV for the hydrogenation of $N_2$ and $NNH_2$, respectively) between the $O_v$ model and the model containing A-site deficiency and oxygen vacancy, we believe that, mainly because of the same adsorption sites, the reaction mechanism could not be changed and using the $O_v$ model to approximate the model containing A-site deficiency and oxygen vacancy is reasonable.

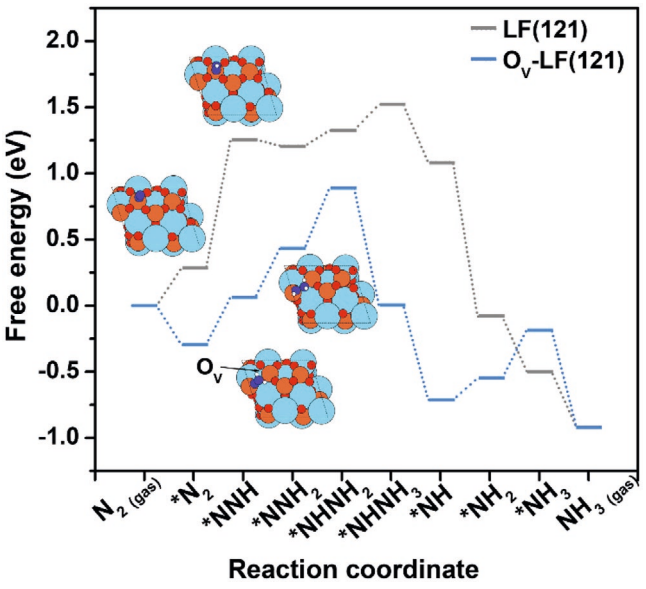


**Figure 5.** Gibbs free energy diagrams for the NRR over the LF(121) surface without/with oxygen vacancy through alternating pathways.

We also demonstrated the generality of this strategy by introducing A-site deficiency in other representative perovskite oxides, including SCF versus $S_{0.95}$CF, and SFT versus $S_{0.95}$FT

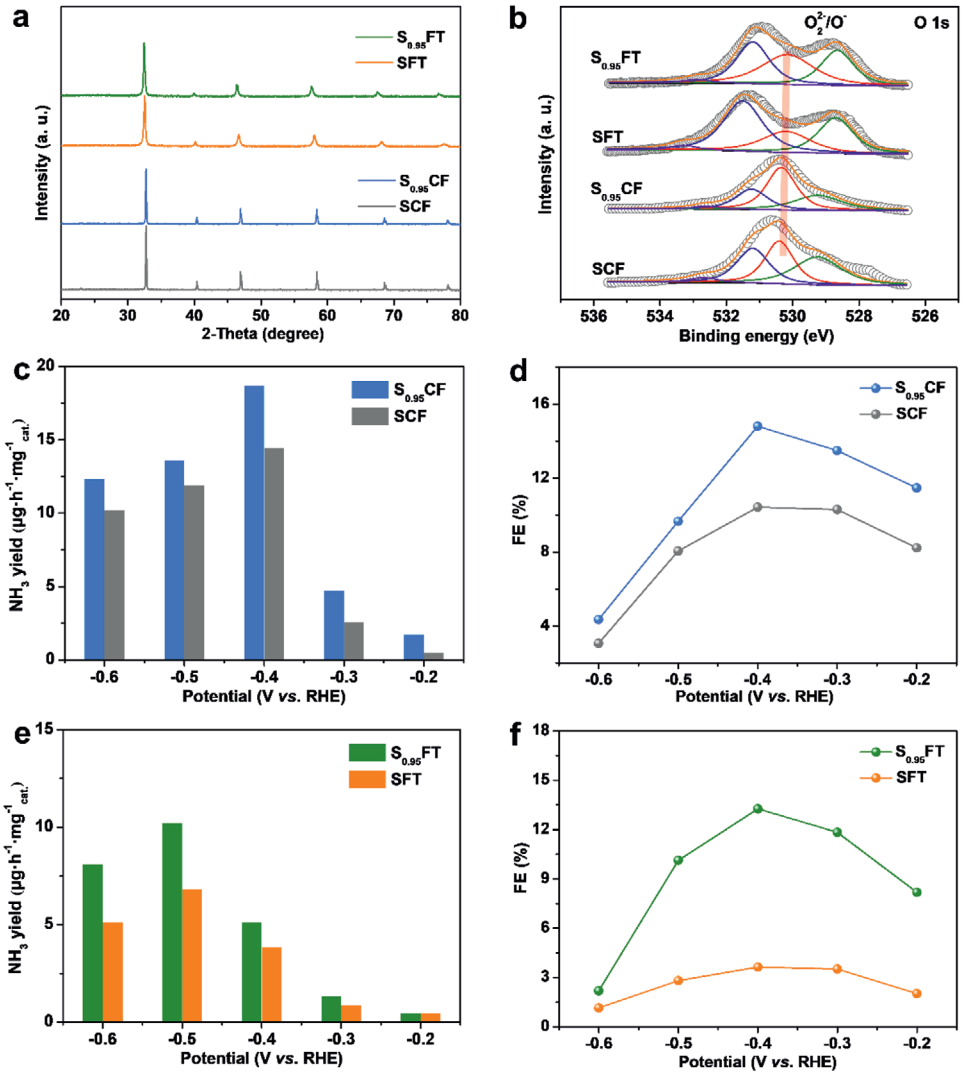


**Figure 6.** a) XRD patterns and b) O 1s spectra of SCF, $S_{0.95}$CF, SFT, and $S_{0.95}$FT. c) Yield rates and d) FEs of $NH_3$ at applied potentials over the SCF and $S_{0.95}$CF. e) Yield rates and f) FEs of $NH_3$ at applied potentials over the SFT and $S_{0.95}$FT catalysts.

nanoparticles (Table S1 and Figure S18, Supporting Information). As shown in **Figure 6**a, all of these samples exhibited pure perovskite phases.[39,40] XPS analyses suggested that, after introducing A-site deficiency, more oxygen vacancies were generated in the $S_{0.95}$CF and $S_{0.95}$FT (Figure 6b). As expected, when tested as NRR catalysts (Figures S19–21, Supporting Information), the $S_{0.95}$CF and $S_{0.95}$FT with extra oxygen vacancies outperformed the pristine SCF and SFT (Figure 6c–f). For instance, relative to SFT (6.8 $\mu g \cdot h^{-1} \cdot mg^{-1}_{cat.}$ and 3.6%), the $S_{0.95}$FT showed great enhancements (1.5- and 3.6-folds, respectively) in terms of $NH_3$ yield rate (10.2 $\mu g \cdot h^{-1} \cdot mg^{-1}_{cat.}$) at –0.5 V and FE (13.3%) at –0.4 V. Therefore, for perovskite oxides, establishing more oxygen vacancies through engineering their A-site deficiency could be a general strategy to boost the activity toward NRR. In Table S5, Supporting Information, we also compared the NRR activities of all the samples in this work with those of other perovskite oxides in the literatures.[14–19] Our samples performed comparably to or better than those reported perovskite oxides except for $LaCoO_{3-\delta}$ that exhibited the highest NRR activities reported so far.

## 3. Conclusion

We have demonstrated that tuning the oxygen vacancies induced by A-site deficiency is a general strategy for enhancing the electrocatalytic NRR activity of perovskite oxides. For the proof-of-concept study, we have prepared a set of perovskite oxide nanoparticles via controlling the La-site deficiencies, including LF, $L_{0.95}$F, and $L_{0.9}$F, which feature adjustable quantity of oxygen vacancies directly proportional to the La-site deficiencies. The NRR activities of the LF, $L_{0.95}$F, and $L_{0.9}$F nanoparticles showed a positive correlation with the amount of their oxygen vacancies. Among the samples, the $L_{0.9}$F with the highest content of oxygen vacancies exhibited the maximal activity and excellent durability toward NRR. Both the experimental characterizations and theoretical calculations indicated that the improved NRR activity could be attributed to the remarkable merits (brought by the oxygen vacancies), that is, the promoted adsorption and activation of reaction species and thus optimized reaction pathways. Moreover, successful

attempts were also made on other perovskite oxides. This work opens the door to the rational design of perovskite oxides for use as highly efficient electrocatalysts toward NRR.

## Supporting Information

Supporting Information is available from the Wiley Online Library or from the author.

## Acknowledgements

K.C. and F.L. contributed equally to this work. The authors are grateful for the financial support from the National Natural Science Foundation of China (51433001), the Shanghai Scientific and Technological Innovation Project (18JC1410600), and the Program of Shanghai Academic Research Leader (17XD1400100). DFT calculations were performed using the HPC Platform of Xi'an Jiaotong University.

## Conflict of Interest

The authors declare no conflict of interest.

## Data Availability Statement

Research data are not shared.

## Keywords

cation deficiency, electrocatalytic $N_2$ reduction, oxygen vacancy, perovskite oxide

Received: December 8, 2020
Revised: January 11, 2021
Published online: January 29, 2021

[1] R. Schlögl, *Angew. Chem., Int. Ed.* **2003**, *42*, 2004.
[2] T. Spatzal, K. A. Perez, O. Einsle, J. B. Howard, D. C. Rees, *Science* **2014**, *345*, 1620.
[3] A. Klerke, C. H. Christensen, J. K. Nørskov, T. Vegge, *J. Mater. Chem.* **2008**, *18*, 2304.
[4] X. Cui, C. Tang, Q. Zhang, *Adv. Energy Mater.* **2018**, *8*, 1800369.
[5] M. Kitano, Y. Inoue, Y. Yamazaki, F. Hayashi, S. Kanbara, S. Matsuishi, T. Yokoyama, S.-W. Kim, M. Hara, H. Hosono, *Nat. Chem.* **2012**, *4*, 934.
[6] M. Ali, F. Zhou, K. Chen, C. Kotzur, C. Xiao, L. Bourgeois, X. Zhang, D. R. MacFarlane, *Nat. Commun.* **2016**, *7*, 11335.
[7] C. Guo, J. Ran, A. Vasileff, S. Qiao, *Energy Environ. Sci.* **2018**, *11*, 45.
[8] Y. Luo, G.-F. Chen, L. Ding, X. Chen, L.-X. Ding, H. Wang, *Joule* **2019**, *3*, 279.
[9] J. Deng, J. A. Iñiguez, C. Liu, *Joule* **2018**, *2*, 846.
[10] L. Zhang, X. Q. Ji, X. Ren, Y. J. Ma, X. F. Shi, Z. Q. Tian, A. M. Asiri, L. Chen, B. Tang, X. P. Sun, *Adv. Mater.* **2018**, *30*, 1800191.
[11] H. Jin, L. Li, X. Liu, C. Tang, W. Xu, S. Chen, L. Song, Y. Zheng, S. Qiao, *Adv. Mater.* **2019**, *31*, 1902709.
[12] J. Wang, B. Huang, Y. Ji, M. Sun, T. Wu, R. Yin, X. Zhu, Y. Li, Q. Shao, X. Huang, *Adv. Mater.* **2020**, *32*, 1907112.
[13] C. Yang, Y. Zhu, J. Liu, Y. Qin, H. Wang, H. Liu, Y. Chen, Z. Zhang, W. Hua, *Nano Energy* **2020**, *77*, 105126.
[14] Y. Liu, X. Kong, X. Guo, Q. Li, J. Ke, R. Wang, Q. Li, Z. Geng, J. Zeng, *ACS Catal.* **2020**, *10*, 1077.
[15] M. Ohrelius, H. Guo, H. Xian, G. Yu, A. A. Alshehri, K. A. Alzahrani, T. Li, M. Andersson, *ChemCatChem* **2020**, *12*, 731.
[16] C. Li, D. Ma, S. Mou, Y. Luo, B. Ma, S. Lu, G. Cui, Q.Li, Q. L., X. Sun, *J. Energy Chem.* **2020**, *50*, 402.
[17] J. Yu, C. Li, B. Li, X. Zhu, R. Zhang, L. Ji, D. Tang, A. M. Asiri, X. Sun, Q. Li, S. Liu, Y. Luo, *Chem. Commun.* **2019**, *55*, 6401.
[18] X. Hu, Y. Sun, S. Guo, J. Sun, Y. Fu, S. Chen, S. Zhang, J. Zhu, *Appl. Catal. B, Environ.* **2021**, *280*, 119419.
[19] S. Zhang, G. Duan, L. Qiao, Y. Tang, Y. Chen, Y. Sun, P. Wan, S. Zhang, *Ind. Eng. Chem. Res.* **2019**, *58*, 8935.
[20] Y. Fang, Z. Liu, J. Han, Z. Jin, Y. Han, F. Wang, Y. Niu, Y. Wu, Y. Xu, *Adv. Energy Mater.* **2019**, *9*, 1803406.
[21] Y. Zhu, H. Tahini, Z. Hu, J. Dai, Y. Chen, H. Sun, W. Zhou, M. Liu, S. Smith, H. Wang, Z. Shao, *Nat. Commun.* **2019**, *10*, 149.
[22] J. Dai, Y. Zhu, H. Tahini, Q. Lin, Y. Chen, D. Guan, C. Zhou, Z. Hu, H. Lin, T. Chan, C. Chen, S. Smith, H. Wang, W. Zhou, Z. Shao, *Nat. Commun.* **2020**, *11*, 5657.
[23] Y. Zhu, H. Tahini, Z. Hu, Z. Chen, W. Zhou, A. Komarek, Q. Lin, H. Lin, C. Chen, Y. Zhong, M. Fernández-Díaz, S. Smith, H. Wang, M. Liu, Z. Shao, *Adv. Mater.* **2020**, *32*, 1905025.
[24] S. Zhang, C. Zhao, Y. Liu, W. Li, J. Wang, G. Wang, Y. Zhang, H. Zhang, H. Zhao, *Chem. Commun.* **2019**, *55*, 2952.
[25] Y. Zhu, Q. Lin, Y. Zhong, H. Tahini, Z. Shao, H. Wang, *Energy Environ. Sci.* **2020**, *13*, 3361.
[26] J. Zhu, G. Liu, Z. Liu, Z. Chu, W. Jin, N. Xu, *Adv. Mater.* **2016**, *28*, 3511.
[27] W. Kong, R. Zhang, X. Zhang, L. Ji, G. Yu, T. Wang, Y. Luo, X. Shi, Y. Xu, X. Sun, *Nanoscale* **2019**, *11*, 19274.
[28] J.-X. Yao, D. Bao, Q. Zhang, M.-M. Shi, Y. Wang, R. Gao, J.-M. Yan, Q. Jiang, *Small Methods* **2019**, *3*, 1800333.
[29] X. Dong, W. Jin, N. Xu, *Chem. Mater.* **2010**, *22*, 3610.
[30] S. Royer, D. Duprez, F. Can, X. Courtois, C. Batiot-Dupeyrat, S. Laassiri, H. Alamdari, *Chem. Rev.* **2014**, *114*, 10292.
[31] Y. Zhu, Z. Chen, W. Zhou, S. Jiang, J. Zou, Z. Shao, *ChemSusChem* **2013**, *6*, 2249.
[32] M. Choi, T. Kim, J. Kim, T. Lee, S. Lee, C. Kim, K. Hong, C. Bark, K. Ko, H. Jang, *Nano Lett.* **2020**, *20*, 8040.
[33] Y. Zhu, W. Zhou, J. Yu, Y. Chen, M. Liu, Z. Shao, *Chem. Mater.* **2016**, *28*, 1691.
[34] Y. Cong, Z. Geng, Y. Sun, L. Yuan, X. Wang, X. Zhang, L. Wang, W. Zhang, K. Huang, S. Feng, *ACS Appl. Mater. Interfaces* **2018**, *10*, 25465.
[35] B. Hammer, J. K. Nørskov, *Adv. Catal.* **2000**, *45*, 71.
[36] J. K. Nørskov, T. Bligaard, J. Rossmeisl, C. H. Christensen, *Nat. Chem.* **2009**, *1*, 37.
[37] C. Yang, B. Huang, S. Bai, Y. Feng, Q. Shao, X. Huang, *Adv. Mater.* **2020**, *32*, 2001267.
[38] B. Comer, A. Medford, *ACS Sustainable Chem. Eng.* **2018**, *6*, 4648.
[39] Q. Lin, Y. Zhu, Z. Hu, Y. Yin, H. -J. Lin, C.- T. Chen, X. Zhang, Z. Shao, H. Wang, *J. Mater. Chem. A* **2020**, *8*, 6480.
[40] J. Zhu, S. Guo, Z. Chua, W. Jin, *J. Mater. Chem. A* **2015**, *3*, 22564.